

# Exploring the Limits of Superconductivity in Metal-Stuffed B-C Clathrates via Ionic Lattice Anharmonicity

Wenbo Zhao,<sup>1,2,†</sup> Ying Sun,<sup>1,2,†</sup> Jiaxiang Li,<sup>1</sup> Peng Yuan,<sup>3</sup> Toshiaki Iitaka,<sup>4</sup> Xin Zhong,<sup>1</sup>  
Hefei Li,<sup>1,5,\*</sup> Yue-Wen Fang,<sup>6,7,‡</sup> Hanyu Liu,<sup>1,2,§</sup> Ion Errea,<sup>6,7,8</sup> and Yu Xie<sup>1,9,¶</sup>

<sup>1</sup>Key Laboratory of Material Simulation Methods and Software of Ministry of Education,  
College of Physics, Jilin University, Changchun 130012, China

<sup>2</sup>International Center of Future Science, Jilin University, Changchun 130012, China

<sup>3</sup>College of Physics, Jilin University, Changchun 130012, China

<sup>4</sup>Discrete Event Simulation Research Team, RIKEN Center for

Computational Science, 2-1 Hirosawa, Wako, Saitama, 351-0198, Japan

<sup>5</sup>State Key Laboratory of Superhard Materials, College of Physics, Jilin University, Changchun 130012, China

<sup>6</sup>Fisika Aplikatua Saila, Gipuzkoako Ingeniaritza Eskola,

University of the Basque Country (UPV/EHU), Europa Plaza 1, 20018 Donostia/San Sebastián, Spain

<sup>7</sup>Centro de Física de Materiales (CSIC-UPV/EHU),

Manuel de Lardizabal Pasealekua 5, 20018 Donostia/San Sebastián, Spain

<sup>8</sup>Donostia International Physics Center (DIPC),

Manuel de Lardizabal Pasealekua 4, 20018 Donostia/San Sebastián, Spain

<sup>9</sup>Key Laboratory of Physics and Technology for Advanced Batteries of Ministry of Education,  
College of Physics, Jilin University, Changchun 130012, China

(Dated: January 22, 2025)

Metal-stuffed B–C compounds with sodalite clathrate structure have captured increasing attention due to their predicted exceptional superconductivity above liquid nitrogen temperature at ambient pressure. However, by neglecting the quantum lattice anharmonicity, the existing studies may result in an incomplete understanding of such a lightweight system. Here, using state-of-the-art *ab initio* methods incorporating quantum effects and machine learning potentials, we revisit the properties of a series of  $XYB_6C_6$  clathrates where  $X$  and  $Y$  are metals. Our findings show that ionic quantum and anharmonic effects can harden the  $E_g$  and  $E_u$  vibrational modes, enabling the dynamical stability of 15 materials previously considered unstable in the harmonic approximation, including materials with previously unreported  $(XY)^{1+}$  state, which is demonstrated here to be crucial to reach high critical temperatures. Further calculations based on the isotropic Migdal-Eliashberg equation demonstrate that the  $T_c$  values for  $KRbB_6C_6$  and  $RbB_3C_3$  among these stabilized compounds are 87 and 98 K at 0 and 15 GPa, respectively, both being higher than  $T_c$  of 77 K of  $KPbB_6C_6$  at the anharmonic level. These record-high  $T_c$  values, surpassing liquid nitrogen temperatures, emphasize the importance of anharmonic effects in stabilizing B–C clathrates with large electron-phonon coupling strength and advancing the search for high- $T_c$  superconductivity at (near) ambient pressure.

## I. INTRODUCTION

The quest for high-temperature superconductivity has predominantly centered on unconventional superconductors for nearly four decades following the discovery of cuprates[1]. However, recent theoretical-driven experimental observations of superconducting critical temperature  $T_c > 200$  K in superhydrides gradually refocus the attention to conventional superconductors[2–5]. In these materials, electrons are coupled via phonons, as elucidated by the Bardeen-Cooper-Schrieffer (BCS) theory[6, 7], which offers an excellent platform for the theoretical design of high-temperature superconductors. Unfortunately, experimental realization of high-temperature superconductivity in superhydrides typically requires high pressures exceeding 150 GPa, which strictly forbids their practical applications[3]. Despite significant efforts to design high- $T_c$  superhydrides at reduced pressures, none of these proposed compounds have been realized experimentally below 50 GPa[3]. Thus, searching for synthesizable

superconductors with high- $T_c$  at low or close to ambient pressure remains an immediate yet challenging task.

Light-element-based covalent metals were regarded as potential high- $T_c$  superconductors at near ambient pressure because the presence of metallic covalent bonds could lead to large phonon frequencies, significant electron-phonon coupling (EPC)[8], and high density of the states at Fermi level ( $N(E_f)$ ), which are the most critical factors for conventional superconductivity[6, 7].  $MgB_2$  with a  $T_c$  of 39 K[9], resulting from a strong coupling of  $\sigma$ -bonding electrons with in-plane B–B vibrational phonons, is the best example of this concept, which holds the record of  $T_c$  among the conventional superconductors at ambient pressure. Other covalent superconductors with lower  $T_c$ s are also observed experimentally[10–13]. Based on this principle, several high- $T_c$  superconductor candidates were proposed, including heavily boron-doped diamond[14], boron-doped graphane[15], doped carbon clathrates[16], layered metal borocarbides[17, 18], B–C compounds[19,

20], and  $\text{SrB}_3\text{C}_3$ [21, 22]. Remarkably, boron appears in almost all materials, serving as a hole dopant to metalize the filled  $\sigma$  carbon bonds while maintaining large EPC and high phonon modes through boron-carbon bonding.

A remarkable recent achievement in the field is that  $\text{SrB}_3\text{C}_3$  has been successfully synthesized at 57 GPa and 2500 K [22], and the predicted superconductivity is also confirmed with an onset  $T_c$  of 20 K at 40 GPa[21, 22]. Superconductivity originates from the interplay between  $\sigma$  B–C bonds and boron  $E_g$  phonon modes[21–23]. The thermodynamically stable range of  $\text{SrB}_3\text{C}_3$  is from 50 to 200 GPa[21, 22], but there is experimental evidence that it may survive close to ambient pressure, where its superconducting  $T_c$  approximates 41 K[22], comparable to  $\text{MgB}_2$ [9]. Notably,  $\text{SrB}_3\text{C}_3$  resembles a host-guest structure, where the metal atom is encapsulated within the B–C cage, offering an excellent opportunity to adjust the properties by varying the stuffed metal atom[21, 22, 24–28]. The subsequently synthesized insulating  $\text{LaB}_3\text{C}_3$ [29] has confirmed that for metal-stuffed B–C clathrates, the shape of the density of states (DOS) remains unchanged, and the metal atom’s valence state determines the Fermi level. Therefore, adjusting the metal’s valence state to position the Fermi level at the DOS peaks can further enhance the superconductivity of metal-stuffed B–C clathrates.

It has been predicted that the superconducting critical temperature can be further enhanced by substituting  $\text{Sr}^{2+}$  with two metal atoms  $X$  and  $Y$  in 1:1 ratio, with many different valence states ( $(XY)^{n+} = \frac{X^{m+} + Y^{l+}}{2}$ ) [24–27]. Most of the designed high- $T_c$   $XY\text{B}_6\text{C}_6$  compounds have an average metal valence state of +1.5, where  $\text{KPbB}_6\text{C}_6$  currently shows the highest predicted  $T_c$  of 88 K[27]. Although the  $T_c$  has been doubled in comparison with that of  $\text{MgB}_2$ , many  $XY\text{B}_6\text{C}_6$  compounds with a Fermi level positioned at the DOS peak, particularly those with an average metal valence state of +1, were predicted to be dynamically unstable. However, the light-weight nature of  $XY\text{B}_6\text{C}_6$  compounds suggests that quantum lattice anharmonicity should play a crucial role in determining their dynamic and superconducting properties[28, 30, 31], because the standard harmonic approximation may not adequately represent the Born-Oppenheimer energy surface in the range defined by the zero point energy. Thus, to gain a unified understanding of the superconductivity in metal-stuffed B–C clathrates, it is an urgent and necessary task to investigate these compounds under the inclusion of anharmonic effects.

Here, we re-examine the dynamical stability and superconductivity of metal-stuffed B–C clathrates ( $X^{n+}[\text{B}_3\text{C}_3]^{n-}$ ,  $X$  can be a single metal or two metals,  $n$  denotes the average valence state) by including quantum lattice anharmonic effects within the stochastic self-consistent harmonic approximation (SSCHA)[32–36]. Meanwhile, an attention-centered neural network

was employed to construct machine learning potentials to address the high computational cost of SSCHA. Our results reveal that anharmonic effects can modify the stability of metal-stuffed B–C clathrates with different metal valence states, allowing us to identify 15 new stable clathrate compounds, including 3  $X^{1+}[\text{B}_3\text{C}_3]^{1-}$  compounds. Our in-depth analysis shows that the average valence state of plus one is the most convenient for high-temperature superconductivity. By utilizing the Migdal-Eliashberg formalism[37–39], we confirm  $X^{1+}[\text{B}_3\text{C}_3]^{1-}$  compounds to have a higher  $T_c$  than that of  $X^{1.5+}[\text{B}_3\text{C}_3]^{1.5-}$  materials. The predicted  $T_c$  is 87 K for  $\text{KRbB}_6\text{C}_6$  at 0 GPa and 98 K for  $\text{RbB}_3\text{C}_3$  at 15 GPa. This is a significant increase of  $\sim 22\%$  compared to the 77 K estimated in  $\text{KPbB}_6\text{C}_6$  at the anharmonic level, establishing the highest possible  $T_c$  value for metal-stuffed B–C clathrates.

## II. RESULTS

We first examine the DOS of  $XY\text{B}_6\text{C}_6$  compounds as shown in Figure 1. The DOS at the Fermi level ( $N(E_f)$ ) is primarily contributed by the B–C framework, with negligible impact from the metal atoms as observed in previous reports[26, 27]. Different metal atom combinations position the Fermi level differently. When the average valence state of metal atoms is +1, +1.5, or +2.25, the Fermi level aligns with DOS peaks (Figure 1b), indicating the potential for high- $T_c$  superconductivity. We need to mention that +2.25 average metal state can only be achieved in  $X_3Y\text{B}_{12}\text{C}_{12}$  compounds[24] with a larger supercell. Moreover, the height of the +2.25 DOS peak is almost the same as the +1.5 DOS peak and lower than the +1 DOS peak. Thus, we focus on the properties of  $XY\text{B}_6\text{C}_6$  compounds with +1 and +1.5 average metal states in the following discussion. The  $N(E_f)$  heat map of  $XY\text{B}_6\text{C}_6$  against metal combinations (Figure 1c) shows clear partitioning due to different metal average valence state. Generally, the  $N(E_f)$  follows the trend  $+1 > +1.5 > +2 \approx +2.5$  with few exceptions, where metal atom Be or Sc is the main contributor to the  $N(E_f)$ . Comparing with the previously reported highest  $N(E_f)$  of  $\text{KPbB}_6\text{C}_6$  (marked as the yellow star), we identify 34  $XY\text{B}_6\text{C}_6$  compounds with larger  $N(E_f)$ , where all of them were predicted to be dynamically unstable at ambient pressure within the harmonic approximation.

Given the low atomic masses of boron and carbon, quantum lattice anharmonic effects might be significant enough to modulate the dynamical properties of  $XY\text{B}_6\text{C}_6$ . We then employ the stochastic self-consistent harmonic approximation (SSCHA) method[33–36] to evaluate the lattice parameter, dynamic stability and superconducting properties of the 34  $XY\text{B}_6\text{C}_6$  compounds with the higher  $N(E_f)$ , where  $\text{SrB}_3\text{C}_3$  and  $\text{KPbB}_6\text{C}_6$  are also considered for better comparison.

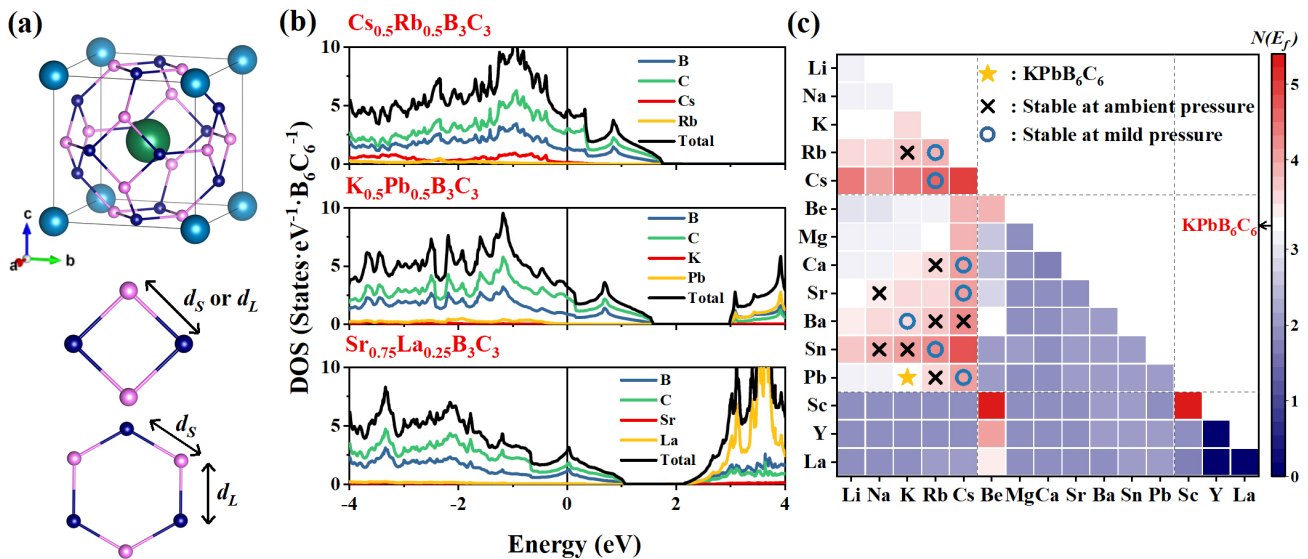


FIG. 1. (a) Crystal structure of  $XYB_6C_6$ , where light blue and green spheres represent metal atoms ( $X$  and  $Y$ ), and pink and dark blue spheres represent B and C atoms, respectively. (b) Projected electronic density of states (PDOS) for the  $Cs_{0.5}Rb_{0.5}B_3C_3$ ,  $K_{0.5}Pb_{0.5}B_3C_3$  and  $Sr_{0.75}La_{0.25}B_3C_3$ [24]. Vertical lines indicate the Fermi level. (c) The heat map in lower triangle shows the density of states at the Fermi level,  $N(E_f)$ , in units of  $states \cdot eV^{-1} \cdot B_6C_6^{-1}$  for various  $XYB_6C_6$  combinations at ambient pressure. Metals  $X$  and  $Y$  are on the x- and y-axes. The color scale is centered on  $KPbB_6C_6$  (yellow star), shown in white. Combinations with higher  $N(E_f)$  are red, and those with lower values are blue. Black crosses indicate dynamically stable combinations at ambient pressure considering anharmonic effects, and pink hexagons show stability under mild pressure (20 GPa). Black dashed lines separate combinations based on the average valence state of the metals.

Notably, the SSCHA method is a rigorous variational approach that directly obtains the anharmonic dynamical matrix by minimizing the quantum free energy functional, achieved stochastically via Monte Carlo summation and importance sampling[40, 41] over several consecutive ensembles (populations) of a large number of individuals ( $N_c$ )[33–36]. However, the method is computationally demanding, particularly for slowly converging soft modes, which often require multiple iterations with population sizes ranging from tens to hundreds of thousands. To address this issue, we develop an SSCHA-ACNN (attention-centered neural network) workflow that employs machine learning potentials (MLPs) and active learning to accelerate the simulations (details of the SSCHA-ACNN workflow and feasibility tests provided in the Supplementary Materials).

The SSCHA-ACNN workflow begins with DFT-level calculations to refine the anharmonic energy surface (AES) and generate a dataset for subsequent MLP-level calculations. At this stage, 8 materials exhibit phonon dispersions without imaginary frequencies (Figures S20–S21), suggesting that they become dynamically stable at ambient pressure due to the inclusion of quantum lattice anharmonic effects. For the remaining materials, we proceed with MLP-based calculations, increasing the number of individual configurations in the en-

semble to over 10,000, and find that they are all dynamically unstable at ambient pressure. Among these, 8 materials exhibit stable auxiliary SSCHA dynamical matrices, but their Hessian dynamical matrices still show imaginary frequencies, indicating that the  $Pm\bar{3}$  structure is not a local minimum in the AES. For the other 18 materials, phonon frequency changes during the SSCHA simulations show that some optical phonon frequencies rapidly drop to zero and remain constant as the ensemble size grows. This behavior suggests flat wave functions and weak restoring forces, reflecting the instability of the  $Pm\bar{3}$  structure and a shallow AES with many energetically comparable local minima and nearly barrierless transition paths. Since high pressure is an effective way to tune the dynamic stability of a compound, we conduct additional SSCHA simulations up to 20 GPa, which can be easily achieved in the large-volume press, resulting in 7 more stable compounds (Figure S22).

Since AES is changed upon introducing quantum lattice anharmonic effects, the crystal structure of materials can be modified. The prototype structure of  $XYB_6C_6$  is based on  $2Sr@B_6C_6$  ( $SrB_3C_3$ ), which has a type-VII clathrate framework[22]. This host framework consists of truncated octahedral cages with six four-sided and eight six-sided faces ( $4^66^8$ ). Each cage comprises 24 vertices, alternating between C and B atoms, with an  $X$  or  $Y$

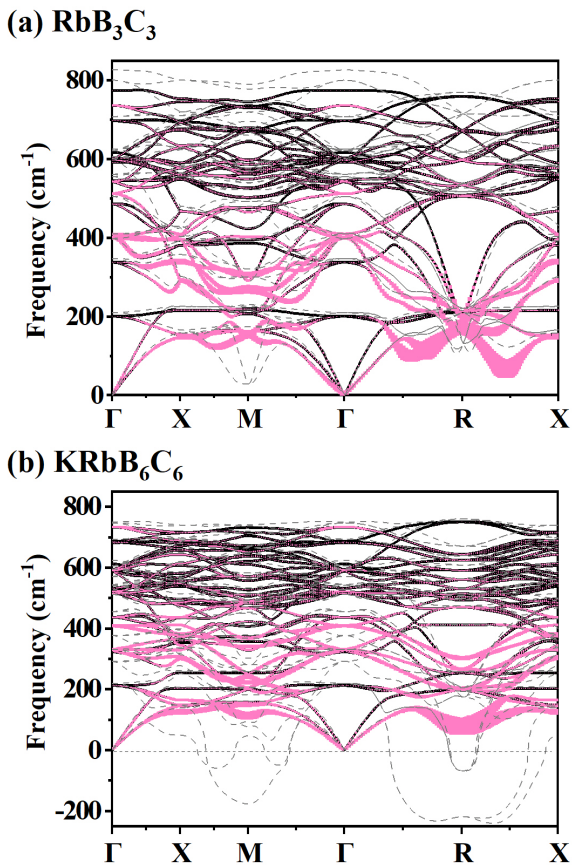


FIG. 2. The gray dashed line represents the harmonic spectrum, and the black solid line represents the anharmonic spectrum obtained from the fourth-order Hessian matrix, where pink solid circles indicate the electron-phonon coupling strength, with the radius proportional to its strength for (a)  $\text{RbB}_3\text{C}_3$  and (b)  $\text{KRbB}_6\text{C}_6$ .

guest cation at the center. When  $X$  and  $Y$  are identical cations ( $\text{XB}_6\text{C}_6$ ), all neighboring B and C atoms have equal bond lengths ( $d_{\text{B-C}}$ ). The anharmonic effect solely increases the lattice parameters of the structure. However, when  $X$  and  $Y$  are different cations, their differences in electric properties and ionic radii create distinct chemical environments around the boron and carbon atoms, resulting in two unequal B–C bond lengths: a longer bond,  $d_{\text{L}}$ , and a shorter bond,  $d_{\text{S}}$ . Our results indicate that anharmonic effects do not alter the lattice symmetry but do increase the lattice parameters and slightly shift the positions of B and C atoms, and enlarge the difference between  $d_{\text{L}}$  and  $d_{\text{S}}$ .

The changes in crystal structure lead to a substantial renormalization of the phonon spectrum at the anharmonic level (Figure 2), particularly evident as an overall softening of the phonon with increasing lattice con-

stant, as well as the softening or hardening of phonon vibrational modes — especially the  $E_g$  and  $E_u$  modes — corresponding to the expansion or contraction of B–C bond lengths. The  $E_g$  mode involves the libration of two boron and two carbon atoms located at opposite corners of the square faces, resulting in the distortion of the quadrilateral into a rectangle, with two B–C edges elongated and two shortened. The  $E_u$  mode features oscillation of the same pairs of boron and carbon atoms at opposite corners, where two atoms move upward and two move downward, altering the symmetry of the face. Both the  $E_g$  and  $E_u$  modes contribute to the distortion of the square faces of the B–C cages, which are key contributors to the instability in  $\text{XYB}_6\text{C}_6$  at the harmonic level.

Anharmonic effects result in longer  $d_{\text{B-C}}$  of  $\text{XB}_6\text{C}_6$  and the expansion in lattice constant, which softens nearly all phonon modes, especially the acoustic branches near the R point, contributing significantly to the electron-phonon coupling (EPC) strength. In contrast, for  $\text{XYB}_6\text{C}_6$ , anharmonic effects increase the difference between  $d_{\text{L}}$  and  $d_{\text{S}}$ . The decrease in  $d_{\text{S}}$  significantly hardens the  $E_g$  and  $E_u$  modes, making eight  $\text{XYB}_6\text{C}_6$  materials dynamically stable at ambient pressure. However, another eight compounds remain unstable because the impact of anharmonic corrections on enhancing the overall stability of certain materials is limited. Among the eight structures that are unstable under ambient pressure and anharmonic effects, seven of them can be stabilized at moderate pressures, as high pressure can reduce the lattice constant and compress the B–C bond length. This compression hardens the phonon modes, thereby enhancing the stability of crystal structures.

According to Eliashberg theory, phonon softening may enhance the electron-phonon coupling, favoring a high  $T_c$ . Anharmonic effects soften the phonon vibration modes of  $\text{XB}_6\text{C}_6$ , so their anharmonic  $T_c$  is usually higher than the harmonic one. For example, the estimated  $T_c$  of  $\text{SrB}_3\text{C}_3$  is renormalized from 19 K (harmonic approximation) to 25 K (anharmonic effects), and that of  $\text{RbB}_6\text{C}_6$  from 93 K to 98 K. For  $\text{XYB}_6\text{C}_6$ , it's more complex. Anharmonic effects soften the acoustic-branch vibration modes related to the lattice constant and harden the  $E_g$  and  $E_u$  vibration modes of the B–C bonds with length  $d_{\text{S}}$ . The latter contributes more to the electron-phonon coupling interaction, making the anharmonic  $T_c$  generally lower than the harmonic one. For instance, the theoretical  $T_c$  of  $\text{KPbB}_6\text{C}_6$  is renormalized from 88 K to 77 K. Furthermore, the maximum anharmonic  $T_c$  value of  $\text{XYB}_6\text{C}_6$  attains 87 K in  $\text{KRbB}_6\text{C}_6$  at ambient pressure, and reaches 98 K in  $\text{RbB}_6\text{C}_6$  at 15 GPa. The  $T_c$  value of 98 K represents a 22 % increase compared to 77 K in  $\text{KPbB}_6\text{C}_6$  at the anharmonic level.

We also analyzed the superconducting mechanisms of 15 newly stabilized structures (Figure 3) — 8 stable at ambient pressure and 7 at moderate pressure — under



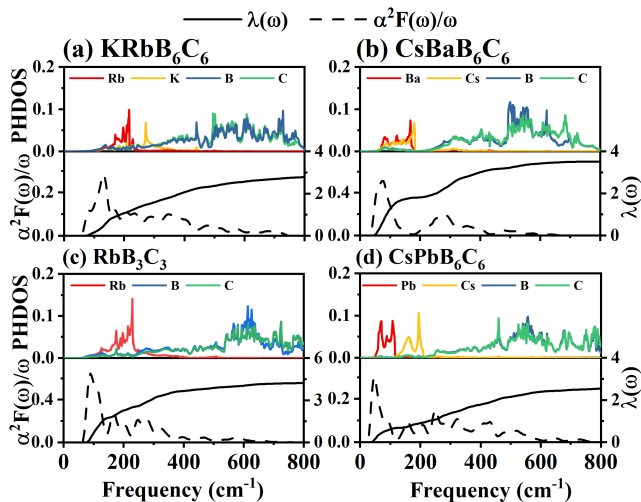


FIG. 3. Projected phonon density of states (PHDOS), Eliashberg spectral function  $\alpha^2 F(\omega)/\omega$  and integral  $\lambda(\omega)$  for (a) KRbB<sub>6</sub>C<sub>6</sub>, (b) CsBaB<sub>6</sub>C<sub>6</sub>, (c) RbB<sub>3</sub>C<sub>3</sub>, (d) CsPbB<sub>6</sub>C<sub>6</sub>.

anharmonic effects. In all studied XYB<sub>6</sub>C<sub>6</sub> compounds, the phonon spectra are divided into two regions based on the phonon frequency: lower-frequency modes (below 200 cm<sup>-1</sup>), which consist of acoustic modes and optical modes dominated by heavier electropositive atoms, and higher-frequency optical modes attributed to boron and carbon atoms. The main contributions to the electron-phonon coupling parameter ( $\lambda$ ) stem from the softened  $E_g$  and  $E_u$  modes, along with the softened acoustic modes. Thus, the lower-frequency modes are critical for enhancing the superconducting properties of XYB<sub>6</sub>C<sub>6</sub> compounds. For instance, in SrNaB<sub>6</sub>C<sub>6</sub> and CaRbB<sub>6</sub>C<sub>6</sub>, the absence of softened acoustic modes reduces their contribution to just 19 % and 25 %, respectively, resulting in a significantly lower  $T_c$  compared to compounds with a higher proportion of these modes (see Supplementary Table 3).

We compared the average valence state of metal atoms, density of states at the Fermi level  $N(E_f)$ , EPC constant  $\lambda$ , logarithmic average phonon frequency  $\omega_{\log}$ , and  $T_c$  values (Figure 4). Our results show that there is no clear linear relationship between  $N(E_f)$  and  $T_c$ . As analyzed in our previous work, the final value of  $T_c$  results from a complex interplay among a high density of states, appropriate phonon energies, and Coulomb repulsion[42]. Instead, the average valence state of metal atoms significantly influences  $T_c$ : compounds with an average valence state of +1 have higher  $T_c$  values than those with +1.5, and materials with the same valence state exhibit similar  $T_c$  ranges due to adjustments in the Fermi level. Valence state of +1 and +1.5 shift the Fermi level to different peaks on either side of a shoulder in the DOS, with the +1 peak slightly higher than the +1.5 peak, explain-

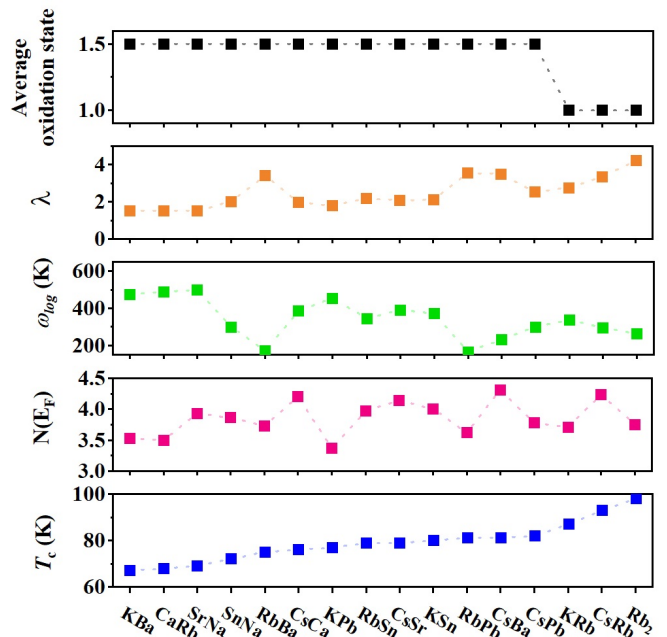


FIG. 4. The average valence state of metal atoms, density of states at the Fermi level  $N(E_f)$ , EPC constant  $\lambda$ , phonon frequency logarithmic average  $\omega_{\log}$ , and superconducting critical temperature  $T_c$  for XYB<sub>6</sub>C<sub>6</sub> compounds.

ing the higher  $T_c$  for +1 compounds. Variations among metal atoms lead to slight differences in peak values for XYB<sub>6</sub>C<sub>6</sub> compounds, making these peaks numerically close and hard to distinguish.

Thermodynamic stability analysis was performed to estimate the synthesis conditions for high-temperature superconducting XYB<sub>6</sub>C<sub>6</sub> compounds, similar to those used for SrB<sub>3</sub>C<sub>3</sub> and LaB<sub>3</sub>C<sub>3</sub>, which can be quenched to ambient conditions after synthesis at mild pressures[21, 22, 29]. Free energy calculations, incorporating decomposition enthalpy relative to the ground-state elemental structures and configurational entropy, were used to provide an upper limit for the pressure and temperature conditions required for XYB<sub>6</sub>C<sub>6</sub> compounds to overcome the enthalpic penalty, same as Geng et al.[27]. The results indicate that 11 out of the 15 newly predicted XYB<sub>6</sub>C<sub>6</sub> compounds exhibit better thermodynamic stability than KPbB<sub>6</sub>C<sub>6</sub> (4000 K and 50 GPa). Notably, the transformation occurs at 4000 K and 20 GPa for KRbB<sub>6</sub>C<sub>6</sub> and at 4000 K and 30 GPa for RbB<sub>3</sub>C<sub>3</sub>, suggesting the possibility of synthesizing these high-temperature superconductors from their elements using laser heating in a diamond anvil cell (see Supporting Information).

### III. CONCLUSION

In summary, this work demonstrates the profound impact of ionic quantum and anharmonic effects on the dynamical stability and superconductivity of B–C clathrate compounds. Fifteen new dynamically stable materials with large electron-phonon coupling constants are identified, including previously unreported materials with +1 average valence state, where quantum fluctuations are essential to sustain their structures. Among these materials, KRbB<sub>6</sub>C<sub>6</sub> and RbB<sub>6</sub>C<sub>6</sub> exhibit critical temperatures of 87 K and 98 K at 0 and 15 GPa, respectively, potentially setting a new record for the highest  $T_c$  among metal-stuffed B–C clathrates. Our results highlight the necessity of accounting for anharmonic and nuclear quantum effects to accurately predict the properties of lightweight materials, which is crucial for designing high-temperature superconductors.

### IV. METHODS

#### DF(P)T calculations

All DFT and DFPT calculations of electronic and vibrational properties were carried out using the plane-wave pseudopotential code Quantum Espresso[43], scalar-relativistic optimized norm-conserving Vanderbilt (ONCV) pseudopotentials[44, 45], and the PBE-GGA exchange and correlation functional[46]. The cutoffs for the wavefunctions and density were chosen as 80 Ry and 640 Ry, respectively. Self-consistent electron density and harmonic phonons were calculated by employing  $24 \times 24 \times 24$   $k$ -point meshes and  $6 \times 6 \times 6$   $q$ -point meshes.

#### SSCHA calculations

Anharmonic effects were estimated using the SSCHA code [33–36] by minimizing the free energy with respect to the average atomic positions  $\mathbf{R}$  and the force constants  $\Phi$ . We used the DFT equilibrium atomic positions and the DFPT dynamical matrix on a  $2 \times 2 \times 2$   $q$ -point grid as the initial guesses for  $\mathbf{R}$  and  $\Phi$ .

The total energy, forces, and stress tensors for each configuration were obtained using DFT in Quantum Espresso[43], combined with machine learning potentials (MLPs) when necessary, as detailed below. At the end of each minimization run, a new ensemble with a larger number of configurations  $N_c$  is generated from the minimized trial density matrix, iterating until convergence. Two stopping criteria were set for the minimization loop: an effective sample size with a Kong–Liu ratio of 0.6, and a ratio of the free energy gradient to the stochastic error of the auxiliary dynamical matrix below  $10^{-6}$ . In DFT-based calculations,  $N_c$  was increased to 1000 configurations, while in the MLP framework it was raised to  $4 \times 10^4$  configurations.

The anharmonic phonon frequencies were obtained from the positional free energy Hessian including the

forth-order terms. The difference between the harmonic and anharmonic dynamical matrices in the  $2 \times 2 \times 2$  phonon-momentum grid was interpolated to a  $6 \times 6 \times 6$  grid. Adding the harmonic  $6 \times 6 \times 6$  grid dynamical matrices to the result, the anharmonic  $6 \times 6 \times 6$   $q$ -grid dynamical matrices were obtained.

#### Machine learning potentials

The machine learning potentials (MLPs) were trained and evaluated using the Attention Coupled Neural Network (ACNN) package. We use Chebyshev polynomial expansions up to the 12th order for radial basis functions within a 6.0 Å cutoff and up to the 10th order for angular functions within a 5.0 Å cutoff.

The MLP was trained on 1000 structures randomly chosen from the last two SSCHA-DFT populations, each containing 1000 structures in a  $2 \times 2 \times 2$  supercell. Separate MLPs were trained for each compound to ensure the highest possible accuracy of our calculations. We validated the potentials on the remaining 1000 structures, finding an RMSE of less than 0.5 meV·atom<sup>-1</sup> for the total energy and less than 50 meV·Å<sup>-1</sup> for the force components. The validations and RMSEs are shown in Supplementary Information.

#### ME theory

The superconducting gap and  $T_c$  values at both the harmonic and anharmonic levels were calculated by numerically solving the isotropic Eliashberg equations[37–39], using values of  $\mu^*$  ranging from 0.1 to 0.15. The Matsubara frequency cutoff is taken to be about 10 times the highest phonon frequency.

### CODE AVAILABILITY

The SSCHA code (<https://github.com/SSCHAcode/python-sscha>) is open source and is based on the GNU General Public License v3.0.

The ACNN code is available from Y. X. upon reasonable request.

### DATA AVAILABILITY

All data in the paper are available from the corresponding author upon request.

### ACKNOWLEDGMENTS

This work was supported by the National Natural Science Foundation of China (Grant No. 12374008, 12022408, 12304013, 12374009, 12074138, 22131006, 52288102, and 52090024), the Interdisciplinary Integration and Innovation Project of JLU, Fundamental Research Funds for the Central Universities and the Program for JLU Science and Technology Innovative Re-

search Team (JLUSTIRT), open project from state key laboratory of superhard materials (No. 202408), and College Student Innovation and Entrepreneurship Training Program (No. S202310183153). I.E. acknowledges financial support from the European Research Council (ERC) under the European Unions Horizon 2020 research and innovation program (Grant Agreement No. 802533), the Spanish Ministry of Science and Innovation (Grant No. PID2022142861NA-I00), the Department of Education, Universities and Research of the Eusko Jaurlaritza and the University of the Basque Country UPV/EHU (Grant No. IT1527-22), and Simons Foundation through the Collaboration on New Frontiers in Superconductivity (Grant No. SFI-MPS-NFS-00006741- 10). Technical and human support provided by DIPC Supercomputing Center is gratefully acknowledged.

### AUTHOR CONTRIBUTIONS

Y. X. designed and supervised the project, W. Z. performed most of the calculations, J. L. assisted with additional calculations, and Y. S. assisted with figure design. All authors contributed to the discussion of the results and participated in preparing the manuscript.

### ETHICS DECLARATIONS

#### Competing interests

The authors declare no competing interests.

### ADDITIONAL INFORMATION

Materials & Correspondence should be addressed to Y.X.

### REFERENCES

- 
- † These two authors contributed equally  
 \* [lihefei37@jlu.edu.cn](mailto:lihefei37@jlu.edu.cn)  
 ‡ [yuewen.fang@ehu.eus](mailto:yuewen.fang@ehu.eus)  
 § [hanyuliu@jlu.edu.cn](mailto:hanyuliu@jlu.edu.cn)  
 ¶ [xieyu@jlu.edu.cn](mailto:xieyu@jlu.edu.cn)
- [1] Bednorz, J. G. & Müller, K. A. Possible high  $T_c$  superconductivity in the Ba-La-Cu-O system. *Zeitschrift für Physik B Condensed Matter* **64**, 189–193 (1986).
  - [2] Lilia, B. *et al.* The 2021 room-temperature superconductivity roadmap. *Journal of Physics: Condensed Matter* **34**, 183002 (2022).
  - [3] Sun, Y., Zhong, X., Liu, H. & Ma, Y. Clathrate metal superhydrides under high-pressure conditions: enroute to room-temperature superconductivity. *National Science Review* **11**, nwad270 (2024). URL <https://doi.org/10.1093/nsr/nwad270>.
  - [4] Zhang, X., Zhao, Y., Li, F. & Yang, G. Pressure-induced hydride superconductors above 200 K. *Matter and Radiation at Extremes* **6** (2021). URL <https://doi.org/10.1063/5.0065287>.
  - [5] Du, M., Zhao, W., Cui, T. & Duan, D. Compressed superhydrides: the road to room temperature superconductivity. *Journal of Physics: Condensed Matter* **34**, 173001 (2022).
  - [6] Ashcroft, N. W. Metallic Hydrogen: A High-Temperature Superconductor? *Physical Review Letters* **21**, 1748–1749 (1968). URL <https://link.aps.org/doi/10.1103/PhysRevLett.21.1748>.
  - [7] Bardeen, J., Cooper, L. N. & Schrieffer, J. R. Theory of Superconductivity. *Physical Review* **108**, 1175–1204 (1957). URL <https://link.aps.org/doi/10.1103/PhysRev.108.1175>.
  - [8] Belli, F., Novoa, T., Contreras-García, J. & Errea, I. Strong correlation between electronic bonding network and critical temperature in hydrogen-based superconductors. *Nature Communications* **12**, 5381 (2021). URL <https://doi.org/10.1038/s41467-021-25687-0>.
  - [9] Nagamatsu, J., Nakagawa, N., Muranaka, T., Zenitani, Y. & Akimitsu, J. Superconductivity at 39 K in magnesium diboride. *Nature* **410**, 63–64 (2001). URL <https://doi.org/10.1038/35065039>.
  - [10] Yamanaka, S. Silicon clathrates and carbon analogs: high pressure synthesis, structure, and superconductivity. *Dalton Transactions* **39**, 1901–1915 (2010).
  - [11] Connétable, D. & Blase, X. Electronic and superconducting properties of silicon and carbon clathrates. *Applied surface science* **226**, 289–297 (2004).
  - [12] Bhaumik, A., Sachan, R., Gupta, S. & Narayan, J. Discovery of high-temperature superconductivity ( $T_c = 55$  K) in B-doped Q-carbon. *ACS nano* **11**, 11915–11922 (2017).
  - [13] Smith, R. P. *et al.* Superconductivity in graphite intercalation compounds. *Physica C: Superconductivity and Its Applications* **514**, 50–58 (2015).
  - [14] Moussa, J. E. & Cohen, M. L. Constraints on  $T_c$  for superconductivity in heavily boron-doped diamond. *Phys. Rev. B* **77**, 064518 (2008). URL <https://link.aps.org/doi/10.1103/PhysRevB.77.064518>.
  - [15] Cheng, Y. *et al.* Superconductivity of boron-doped graphane under high pressure. *RSC advances* **9**, 7680–7686 (2019).
  - [16] Zipoli, F., Bernasconi, M. & Benedek, G. Electron-phonon coupling in halogen-doped carbon clathrates from first principles. *Physical Review B—Condensed Matter and Materials Physics* **74**, 205408 (2006).
  - [17] Tomassetti, C. R., Kaffle, G. P., Marcial, E. T., Margine, E. R. & Kolmogorov, A. N. Prospect of high-temperature superconductivity in layered metal borocarbides. *Journal of Materials Chemistry C* **12**, 4870–4884 (2024).
  - [18] Hayami, W., Rocquefelte, X. & Halet, J.-F. Possible Superconductivity for Layered Metal Boride Carbide Compounds MB<sub>2</sub>C<sub>2</sub> (M= Alkali, Alkaline-Earth, or Rare-Earth Metals). *Inorganic Chemistry* (2024).
  - [19] Li, Q. *et al.* Superhard and superconducting structures of BC<sub>5</sub>. *Journal of Applied Physics* **108** (2010). URL <https://doi.org/10.1063/1.3452374>.

- [20] Saha, S., Di Cataldo, S., Amsler, M., Von Der Linden, W. & Boeri, L. High-temperature conventional superconductivity in the boron-carbon system: Material trends. *Physical Review B* **102**, 024519 (2020).
- [21] Zhu, L. *et al.* Superconductivity in SrB<sub>3</sub>C<sub>3</sub> clathrate. *Physical Review Research* **5**, 013012 (2023). URL <https://link.aps.org/doi/10.1103/PhysRevResearch.5.013012>.
- [22] Zhu, L. *et al.* Carbon-boron clathrates as a new class of sp<sup>3</sup>-bonded framework materials. *Science Advances* **6**, eaay8361. URL <https://doi.org/10.1126/sciadv.aay8361>.
- [23] Wang, J.-N., Yan, X.-W. & Gao, M. High-temperature superconductivity in SrB<sub>3</sub>C<sub>3</sub> and BaB<sub>3</sub>C<sub>3</sub> predicted from first-principles anisotropic Migdal-Eliashberg theory. *Physical Review B* **103**, 144515 (2021). URL <https://link.aps.org/doi/10.1103/PhysRevB.103.144515>.
- [24] Gai, T.-T. *et al.* Van Hove singularity induced phonon-mediated superconductivity above 77 K in hole-doped SrB<sub>3</sub>C<sub>3</sub>. *Physical Review B* **105**, 224514 (2022). URL <https://link.aps.org/doi/10.1103/PhysRevB.105.224514>.
- [25] Zhang, P. *et al.* Path to high- $T_c$  superconductivity via Rb substitution of guest metal atoms in the SrB<sub>3</sub>C<sub>3</sub> clathrate. *Physical Review B* **105**, 094503 (2022). URL <https://link.aps.org/doi/10.1103/PhysRevB.105.094503>.
- [26] Di Cataldo, S., Qulaghasi, S., Bachelet, G. B. & Boeri, L. High- $T_c$  superconductivity in doped boron-carbon clathrates. *Physical Review B* **105**, 064516 (2022). URL <https://link.aps.org/doi/10.1103/PhysRevB.105.064516><https://journals.aps.org/prb/abstract/10.1103/PhysRevB.105.064516>.
- [27] Geng, N. *et al.* Conventional High-Temperature Superconductivity in Metallic, Covalently Bonded, Binary-Guest C–B Clathrates. *Journal of the American Chemical Society* **145**, 1696–1706 (2023). URL <https://doi.org/10.1021/jacs.2c10089>.
- [28] Sun, Y. & Zhu, L. Hydride Units Filled B–C Clathrate: A New Pathway for High-Temperature Superconductivity at Ambient Pressure. *arXiv preprint arXiv:2311.01656* (2023).
- [29] Strobel, T. A., Zhu, L., Guñka, P. A., Borstad, G. M. & Guerette, M. A Lanthanum-Filled Carbon–Boron Clathrate. *Angewandte Chemie International Edition* **60**, 2877–2881 (2021). URL <https://doi.org/10.1002/anie.202012821>.
- [30] Errea, I. *et al.* Quantum hydrogen-bond symmetrization in the superconducting hydrogen sulfide system. *Nature* **532**, 81–84 (2016). URL <https://doi.org/10.1038/nature17175>.
- [31] Errea, I. *et al.* Quantum crystal structure in the 250-kelvin superconducting lanthanum hydride. *Nature* **578**, 66–69 (2020). URL <https://doi.org/10.1038/s41586-020-1955-z>.
- [32] Monacelli, L. *et al.* The stochastic self-consistent harmonic approximation: calculating vibrational properties of materials with full quantum and anharmonic effects. *Journal of Physics: Condensed Matter* **33**, 363001 (2021). URL <https://dx.doi.org/10.1088/1361-648X/ac066b>.
- [33] Errea, I., Calandra, M. & Mauri, F. First-Principles Theory of Anharmonicity and the Inverse Isotope Effect in Superconducting Palladium-Hydride Compounds. *Phys. Rev. Lett.* **111**, 177002 (2013). URL <https://link.aps.org/doi/10.1103/PhysRevLett.111.177002>.
- [34] Errea, I., Calandra, M. & Mauri, F. Anharmonic free energies and phonon dispersions from the stochastic self-consistent harmonic approximation: Application to platinum and palladium hydrides. *Phys. Rev. B* **89**, 064302 (2014). URL <https://link.aps.org/doi/10.1103/PhysRevB.89.064302>.
- [35] Bianco, R., Errea, I., Paulatto, L., Calandra, M. & Mauri, F. Second-order structural phase transitions, free energy curvature, and temperature-dependent anharmonic phonons in the self-consistent harmonic approximation: Theory and stochastic implementation. *Phys. Rev. B* **96**, 014111 (2017). URL <https://link.aps.org/doi/10.1103/PhysRevB.96.014111>.
- [36] Monacelli, L., Errea, I., Calandra, M. & Mauri, F. Pressure and stress tensor of complex anharmonic crystals within the stochastic self-consistent harmonic approximation. *Phys. Rev. B* **98**, 024106 (2018). URL <https://link.aps.org/doi/10.1103/PhysRevB.98.024106>.
- [37] Eliashberg, G. Interactions between electrons and lattice vibrations in a superconductor. *Sov. Phys. JETP* **11**, 696–702 (1960).
- [38] Giustino, F., Cohen, M. L. & Louie, S. G. Electron-phonon interaction using Wannier functions. *Physical Review B—Condensed Matter and Materials Physics* **76**, 165108 (2007).
- [39] Sanna, A. *et al.* Ab initio Eliashberg theory: making genuine predictions of superconducting features. *Journal of the Physical Society of Japan* **87**, 041012 (2018).
- [40] Neal, R. M. Annealed importance sampling. *Statistics and computing* **11**, 125–139 (2001).
- [41] Martoňák, R. & Tosatti, E. Path-integral Monte Carlo study of a model two-dimensional quantum paraelectric. *Physical Review B* **49**, 12596 (1994).
- [42] Cerqueira, T. F. T., Fang, Y.-W., Errea, I., Sanna, A. & Marques, M. A. L. Searching Materials Space for Hydride Superconductors at Ambient Pressure. *Advanced Functional Materials* **34**, 2404043 (2024).
- [43] Giannozzi, P. *et al.* QUANTUM ESPRESSO: a modular and open-source software project for quantum simulations of materials. *Journal of physics: Condensed matter* **21**, 395502 (2009).
- [44] Schlipf, M. & Gygi, F. Optimization algorithm for the generation of ONCV pseudopotentials. *Computer Physics Communications* **196**, 36–44 (2015). URL <https://www.sciencedirect.com/science/article/pii/S0010465515001897>.
- [45] Hamann, D. R. Optimized norm-conserving Vanderbilt pseudopotentials. *Phys. Rev. B* **88**, 085117 (2013). URL <https://link.aps.org/doi/10.1103/PhysRevB.88.085117>.
- [46] Perdew, J. P., Burke, K. & Ernzerhof, M. Generalized gradient approximation made simple. *Physical review letters* **77**, 3865 (1996).